Ultra-Compact Camera-Integrated Deep-Implanted Two-Port MIMO Antenna for High-Data-Rate Wireless Capsule Endoscopy

Muhammad Qamar, *Student Member, IEEE,* Kamil Yavuz Kapusuz, *Member, IEEE,* Lawrence Carslake, Tian-Hong Loh, *Senior Member, IEEE,* Mohamed A. Thaha, and Akram Alomainy, *Senior Member, IEEE*

***Abstract*—This study proposes a novel high-performance, two-element camera-integrated antenna array for the [401-406] MHz medical device radio communications service (MedRadio) band. The array is designed for integration inside a capsule to establish a stable, high data-rate multiple-input multiple-output (MIMO) wireless communication link for wireless endoscopy. The compact antenna ($\pi\times$ 1.125 $\times$1.49 mm^3) uses stacked meandered resonators, nestled within an annular ring-shaped planar substrate, offering over 7 MHz bandwidth and 41 dB isolation. It achieves a 78 Mbps data rate over 1.6 m in muscle tissue with a specific absorption rate of 2 W/kg at 20 mW power. Measurements show an ECC below 0.001, diversity gain over 9.99 dB, and a channel capacity of 10 bps/Hz at 20 dB SNR. To the best of our knowledge, this is the first dual-camera-integrated MIMO antenna system for the [401-406] MHz MedRadio band tested in an implantable device.**

***Index Terms*—Camera integrated, capsule antenna, implantable medical devices (IMD), meandered resonator, multiple-input-multiple-output (MIMO) antenna, wireless capsule endoscopy (WCE).**

I. Introduction

RECENTLY, the demand for ingestible and implantable medical devices (IMDs) for patient monitoring and diagnosis has surged [1]- [4]. Wireless capsule endoscopy (WCE), in particular, has gained significant attention for its ability to continuously capture and transmit internal body data, images, and videos. Unlike traditional wired solutions that cause discomfort and limit test coverage [5], [6], WCE reduces infections and hazards linked to reusable colonoscopy wires [7], [8]. However, WCE design challenges include providing a wide-angle camera view and maintaining a reliable communication link with an external receiver, whether on or off the body [9], [10]. Consequently, there is a growing need for WCE systems with high data rates, low latency, high reliability, and expansive camera views [11].

To ensure high data rates and mitigate performance degradation due to varied tissue environments, low-frequency multiple-input-multiple-output (MIMO) systems [see Fig. 1(a)] have been proposed for WCE [12]. Small printed antennas are favored for their ease of implementation, cost-effectiveness, and compactness within a capsule. Yet, mutual coupling between MIMO antennas can impact channel parameters. A dual-camera system in WCE improves diagnostic accuracy and outcomes over single-camera systems by capturing front and back views, reducing blind spots [13], [14], and enhancing gastrointestinal (GI) tract coverage [15], [16]. It enhances efficiency [17], [18], reduces repeat procedures [19], [20], and improves patient comfort. Developing ultra-compact, high-performance MIMO antennas that fit into millimeter-sized capsules without obstructing camera views is essential. These antennas should deliver robust performance while being compatible with cost-effective manufacturing.

Extensive research on single-band [21]- [26], multi-band [27]- [34], and wideband [35]- [39] antennas for single-input-single-output (SISO) WCE systems has been carried out, but few MIMO antennas have been proposed. These mainly focus on implementing them capsule edge-embedded [40]-[43] or capsule body-conforming [44]- [46] designs. While edge-embedded antennas offer high RF performance, they limit the integration of dual cameras. Conformal antennas allow for dual cameras but are complex to design and integrate, especially in small capsules. Thus, creating compact, broadband MIMO antenna modules with simple integration for dual-camera WCE remains challenging.

This paper introduces an ultra-compact, camera-integrated two-element MIMO array for in-body capsule applications. The novel design allows (i) easy integration of two cameras (one on each side) and other components without affecting antenna performance, (ii) stable S-parameters and radiation performance across a wide range of biological tissue properties ($\epsilon_{tissue}\in$[10-80], $\sigma_{tissue}\in$[0-2.4] S/m) without additional matching networks, (iii) compatibility with standard PCB manufacturing processes, and (iv) excellent isolation between antennas and components. A proof-of-principle prototype was manufactured using a multilayer PCB process. The prototype covers the [401-406] MHz of the medical device radio communications service (MedRadio) band and ensures isolation greater than 41 dB. Unlike previous designs operating at higher frequencies (e.g., 2.45 GHz) with a *single end-facing camera* [47], this design operates at a lower frequency and integrates dual cameras. Moreover, in contrast to [48], [49], where single camera-integrated antennas are developed to operate at 2.4 GHz industrial, scientific, and medical (ISM) band, *to the authors' knowledge, this is the first* ***dual*** *camera-integrated MIMO antenna system operating in the [401-406] MHz MedRadio band, simulated and measured inside a quasi-implantable device.*

II. Antenna Requirements and Body Modelling

A. Physical Constraints

Fig. 1(a) shows the schematic of the ingestible capsule, which includes two cameras, a transceiver PCB, LEDs, a MIMO antenna module, optical domes, and batteries within a biocompatible shell. The entire implant fits into a pill-shaped

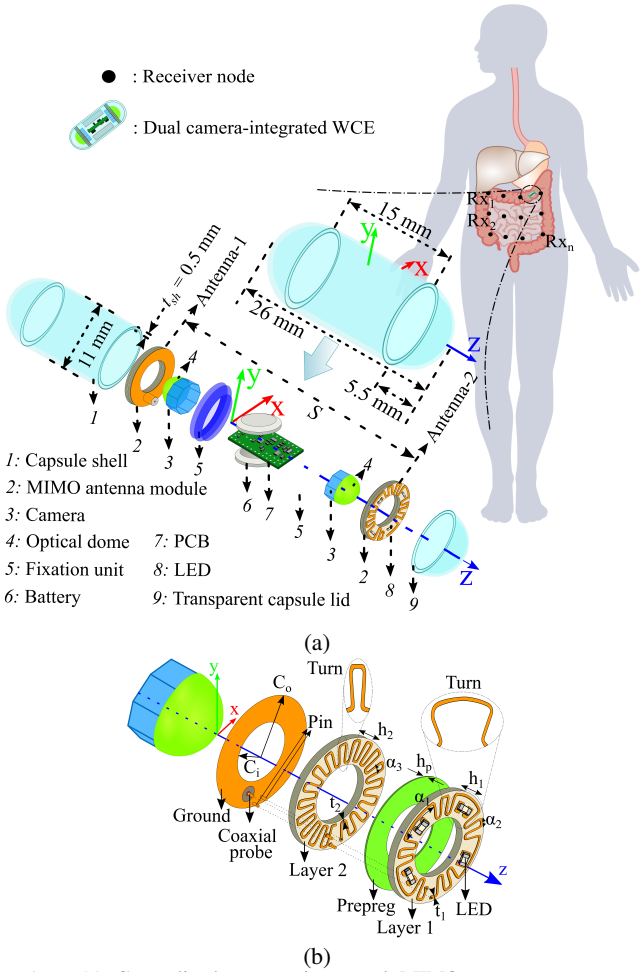

Fig. 1. (a) Generalized camera integrated MIMO antenna system and systematic overview of the proposed WCE. (b) Exploded view of the MIMO unit antenna and its parameterized dimensions. The geometrical dimensions are: C_i = 3.25 mm, C_o = 5.5 mm, t_1 = t_2 = 0.20 mm, α_1 = 40^o, α_2 = α_3 = 10^o, h_1 = h_2 = 0.6435 mm, h_p = 0.135 mm. Substrate parameters at 10.0 GHz: Rogers RO3010 (ϵ_r = 10.2 and tanδ = 0.0022) and prepreg material (ϵ_r = 10.2, and tanδ = 0.01).

housing with a diameter of 11 mm and a height of 26 mm [15]. The shell must prevent adverse tissue reactions and short-circuiting from body tissues [50]. The air gap between the antenna and the transparent capsule lid is crucial for maximizing power transmission to free space [51]. Therefore, compact and efficient packaging is necessary to maintain a small implant volume and clear camera views [10].

B. EM Specifications

As the capsule travels through the GI tract, varying EM properties of different tissues may distort the MIMO antenna performance [52]. To ensure optimal wireless link quality, the design must account for the changing environment. The MIMO antenna must balance robust frequency response, high isolation, and low specific absorption rate (SAR). Key EM specifications for the design include leveraging low frequencies to maximize body penetration [53] and minimize signal attenuation [54]. Commercial capsules typically operate at low frequencies, such as 434 MHz [15]. Each port's reflection coefficient should stay below –10 dB across the [401-406] MHz band [55], with intra-element isolation above 40 dB. The MIMO element should achieve a gain (G) of approximately -50 dBi. To ensure patient safety, SAR values must be less than

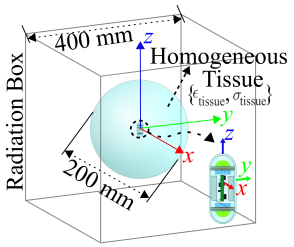

Fig. 2. Problem formulation (not to scale): A capsulated MIMO antenna array is centered inside a homogenized ϕ200 mm spherical phantom, covering the complete range of biological tissue EM properties (ϵ_{tissue}, σ_{tissue}) at 401 MHz. For homogenized muscle phantom, ϵ_{tissue} and σ_{tissue} equal to 56.86 and 0.81 S/m, respectively.

1.6 W/kg over 1-g and 2 W/kg over 10-g of tissue, according to IEEE standards [56], [57].

C. Human Body Modeling

Currently, various human body parts can be modeled with varying complexity [58], [59]. Yet, analyzing the impact of tissue relative dielectric constant (ϵ_{tissue}) and conductivity (σ_{tissue}) on antenna performance requires results independent of phantom geometry. Even though complex shapes and heterogeneities may offer optimal solutions for specific test scenarios, they also introduce shape-related disturbances to the results [60].

To reduce simulation time and ensure shape and heterogeneity independence, this study uses a simple non-resonant homogeneous sphere as a human body model. Although this is a rough approximation, the spherical symmetry allows characterization of radiation performance under controlled isotropic conditions [61]. Unlike the spherical shape, other shapes (such as cylindrical or cubic) may distort antenna performance in terms of directivity. The MIMO array is positioned at the center of a homogeneous sphere phantom, as shown in Fig. 2. A sphere diameter of ø200 mm is chosen for all simulations to represent potential implantation depth, ensuring at least half-wavelength propagation for $f_0 \geq$ 401 MHz and $\epsilon_{tissue} \geq$ 10. For the MedRadio band, the phantom's EM properties are within $\epsilon_{tissue} \in$[10-80] and $\sigma_{tissue} \in$ [0-2.4] S/m [62].

III. Camera-Integrated MIMO Antenna Design

A. Antenna Element

To address various constraints and meet rigorous requirements, we propose an ultra-compact camera-integrated antenna for MIMO communication, shown in Fig. 1(b). Leveraging an annular ring topology, the antenna substrate is seamlessly embedded between the camera and the capsule wall.

The antenna has three copper layers, including the radiating elements and ground plane. It uses two layers of 0.635-mm-thick high dielectric constant RO3010 substrate and one layer of 0.135-mm-thick prepreg. Such a thin high dielectric constant substrate allows a smaller structure while limiting the surface wave excitation, and the low loss tangent minimizes dielectric loss.

To achieve resonance within the MedRadio frequency band, the proposed antenna model undergoes four iterative design steps, as illustrated in Fig. III-A. Fig. III-A(a) shows the magnitude of the reflection coefficient at each stage. The design design starts with creating a multilayer PCB with an annular ring shape. The outer diameter is encased within a

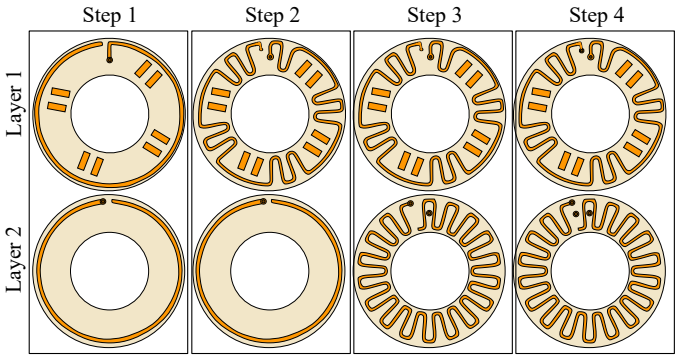

Fig. 3. Design evolution of the antenna: Step 1-Step 4 (proposed antenna).

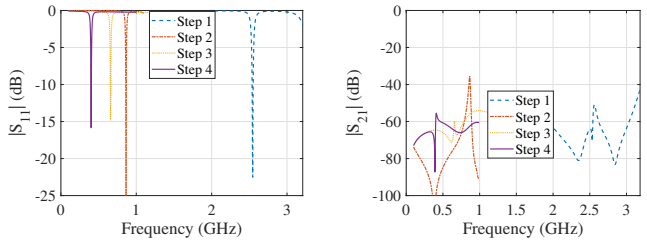

Fig. 4. S-parameters of different design steps: (a) $|S_{11}|$. (b) $|S_{21}|$.

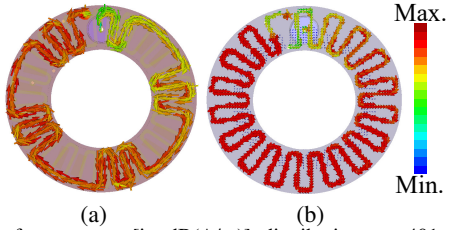

Fig. 5. Surface current [in dB(A/m)] distributions at 401 MHz at antenna 1: (a) Layer 1 and (b) Layer 2.

capsule shell, while an inner hole accommodates the camera. In Step 1, the antenna features a single metal wire with a single bend on each layer, resulting in a resonant frequency of 2.5 GHz. Step 2 involves folding the antenna arm on Layer 1, creating an offset feed [63], [64]. This extends the antenna's electrical length, allowing current to flow along the newly formed radiating elements and reducing the resonant frequency to 860 MHz. In Step 3, additional turns are added to the antenna arm on Layer 2, further reducing the operating frequency of 650 MHz. Finally, Step 4 incorporates shorting pins with a 0.25 mm diameter to achieve an even lower frequency without additional folding. Ultimately, the antenna [see Fig. 1(b)] operates at 401 MHz with a bandwidth of 7 MHz. Numerical optimization in a homogenized muscle phantom (ϵ_{tissue} = 56.86 and σ_{tissue} = 0.81 S/m) ensures the desired 50 Ω input impedance. Fig.5(a) and Fig. 5(b) depict vector current distributions on the meandered lines of antenna-1 on Layer 1 and Layer 2, showing that exciting the port mainly induces surface currents along the meandered microstrip lines.

B. MIMO Array

The MIMO array, shown in Fig. 1(a), includes two identical antenna elements positioned to avoid obstructing the $\pm 70^o$ camera's field of view [65]. This design integrates a dual-camera system within the capsule shell. The antenna PCBs are divided within the capsule to create a distributed MIMO-like

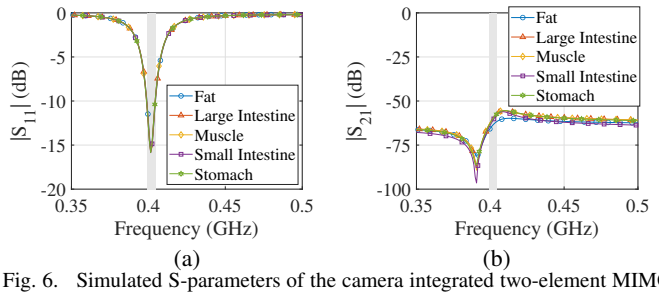

Fig. 6. Simulated S-parameters of the camera integrated two-element MIMO capsule antenna in different tissues. (a) Magnitude of reflection coefficient $|S_{11}|$. (b) Coupling between two MIMO antenna $|S_{21}|$.

configuration [66]. Despite the distributed layout, a common ground is maintained through the PCB and coaxial probe [see Fig. 1(a)], reducing the MIMO channel capacity's dependence on capsule-receiver positioning. To ensure at least 40 dB isolation between antenna elements [see Fig. III-A(b)] and a -10 dB impedance bandwidth across the frequency band during the design process, the distance S between elements is set to 15 mm. Increasing S could improve isolation but would enlarge the capsule, which is undesirable.

IV. EM Performance of Encapsulated MIMO Array

A. Matching and Isolation

1) Robustness to Tissue: The S-parameters of the antenna in MIMO array configurations [see Fig. 1(a)] are initially investigated in the dispersive phantom representing five tissues in the GI tract: fat, muscle, stomach, small and large intestine in the full-wave frequency-domain solver of CST Microwave Studio 2022 [67].

Fig. 6 illustrates the S-parameters performance in various phantoms, including those mimicking the properties of the digestive tract. The results demonstrate consistent reflection coefficient magnitudes and effective isolation between antenna elements across the 401 MHz MedRadio band. The antenna maintains a reflection coefficient below -10 dB from 399 MHz to 407 MHz for fat, muscle, stomach, small and large intestine states, covering the entire [401-406] MHz band with a 2 MHz impedance bandwidth margin [Fig. 6(a)]. Isolation exceeds 57 dB across all tissues in the operational band Fig. 6(b).

Fig. 7 illustrates the antenna's detuning immunity area. Reflection coefficient magnitudes ($|S_{11}|\&|S_{22}|$) remain below -10 dB for all tissues Fig. 7(a), with isolation ($|S_{21}|$) exceeding 45 dB, even with tissue permittivity around 40 and conductivity at 0. Isolation between elements consistently surpasses 55 dB across all phantoms, as shown in Fig. 7(b).

2) Robustness to Capsule Components: In the capsule, all the components, depicted in Fig. 1(a), are carefully placed, each with explicit properties. The cameras and optical domes are placed in the inner hole of the antenna substrate, whereas the transceiver PCB and the batteries are stacked vertically. The components consisted of the following: the transceiver PCB was made of FR4; batteries were modeled as perfect electric conductor (PEC) cylinders with a diameter of 7.9 mm and a height of 2.1 mm; the fixation unit with a diameter of 11 mm made of 2 mm thick Alumina (Al2O3, ϵ_r = 9.8, tan δ = 0.006); electronic components, LEDs and camera were given the properties of silicon (ϵ_r = 11.9, σ = 0.00025 S/m);

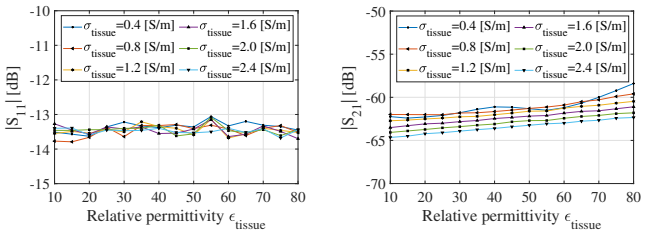

(a) (b)

Fig. 7. (a) Matching ($|S_{11}|$) and (b) mutual coupling ($|S_{21}|$) stability of the proposed camera integrated two-element MIMO antenna simulated at 401 MHz in a homogeneous ø200 mm spherical phantom within the complete

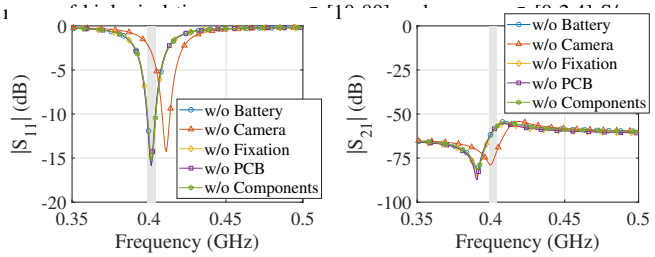

(a) (b)

Fig. 8. Effect of capsule inner components on the S-parameters of the antenna. (a) Magnitude of reflection coefficient $|S_{11}|$. (b) Coupling between two MIMO antenna $|S_{21}|$.

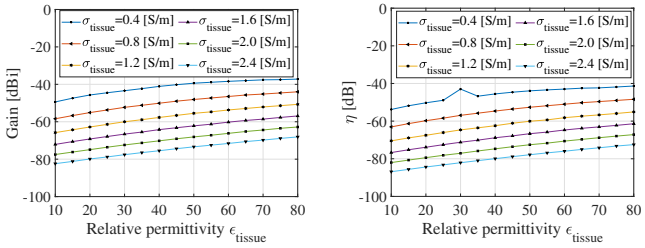

(a) (b)

Fig. 9. (a) Gain (dBi) and (b) efficiency η (dB) stability of the proposed camera integrated two-element MIMO antenna simulated at 401 MHz in a homogeneous ø200 mm spherical phantom within the complete range of biological tissue $\epsilon_{tissue} \in$ [10-80] and $\sigma_{tissue} \in$ [0-2.4] S/m.

a capsule body was given the properties of 3D-printing material of acrylonitrile butadiene styrene (ABS) (ϵ_r = 3.05, tan δ = 0.05); and capsule lids were given the properties of glass material (ϵ_r = 4.7, tan δ = 0.01).

Fig. 8(a) and Fig. 8(b) depict the S-parameters performance of the antenna performance by the presence of nearby components. All the components were included, and a parametric study was conducted to choose the best location for the antennas' placement. The ground planes shield the antennas' from other capsule components, enhancing its resilience. Yet, the absence of the camera shifts the antennas' operating frequencies by around 0.01 MHz.

B. Radiation Performance and SAR

Fig. 9 shows the gain (dBi) and efficiency (dB) of the two-element MIMO antenna across biological tissue parameters $\epsilon_{tissue} \in$[10–80] and $\sigma_{tissue} \in$[0–2.4]S/m. The antenna maintains significant gain and efficiency at a 100 mm implantation depth in various tissues. Notably, in the presence of fat, the gain and efficiency improve to -37 dBi and -42 dB, respectively. However, in the small intestine, both efficiency and gain degrade to -63 dBi and -70 dB due to its high conductivity.

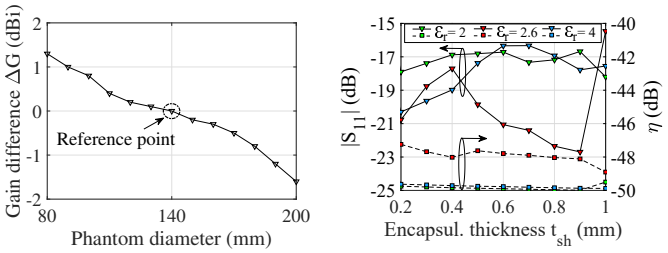

(a) (b)

Fig. 10. (a) Gain difference ΔG of the antenna at 401 MHz, operating within the muscle equivalent phantom of various sizes. (b) Effect of the encapsulation thickness t_{sh} and capsule shell permittivity on simulated reflection coefficient $|S_{11}|$ and total efficiency η at 401 MHz.

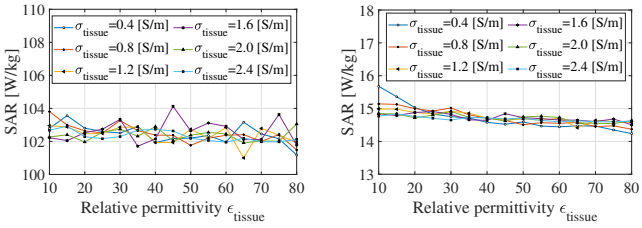

(a) (b)

Fig. 11. SAR (W/kg) covering the complete range of biological tissue EM properties when P_{IN} = 0.5 W. (a) 1-g. (b) 10-g.

Up to this point, the depth of the in-body antenna effects has not been investigated on the antenna radiation performance. In tissue, maximum radiation efficiency at a given frequency is limited by attenuation and high-contrast boundaries like tissue-air interfaces, which affect surface waves and reflections [68], [69]. Fig. 10(a) shows the gain difference ΔG in a muscle-equivalent non-resonant phantom with diameters from 80 mm to 200 mm. As antenna depth in tissue increases, gain decreases due to higher attenuation.

To ensure patient safety, SAR is simulated using the full-wave time-domain solver in CST Microwave Studio2022 [67]. Simulations consider 1-g and 10-g tissue models, with each antenna port driven at 0.5 W input power P_{IN}. At 401 MHz, peak SAR values are 101.5 W/kg for 1-g and 14.4 W/kg for 10-g tissues, as shown in Fig. 11(a) and Fig. 11(b). To comply with safety standards, input power of 165 mW claculted for 1 g tissue and 20 mW for 10 g tissue results in a safe 10 g SAR of 2 W/kg, exceeding the maximum allowable power limit of 25 μW [32].

C. Impact of Capsule Packaging

The antenna and other components were housed in a biocompatible shell measuring 11 mm in diameter and length, created using 3D printing and two transparent capsule lid [see Fig. 1(a)].

The shell's material and thickness significantly impact the antenna's radiation performance by partially decoupling it from surrounding tissues with varying electromagnetic properties [70]. To evaluate this, the shell thickness t_{sh} [see Fig. 1(a)] was varied from 0.2 mm to 1 mm while the shell permittivity ranged from 2 to 4. Fig. 10(b) illustrates the effect on $|S_{11}|$ and the total antenna efficiency η at 401 MHz. The antenna maintains good impedance matching ($|S_{11}| <$ -10 dB), due to the tissue-matched dielectric loading. However, radiation efficiency decreases as t_{sh} increases.

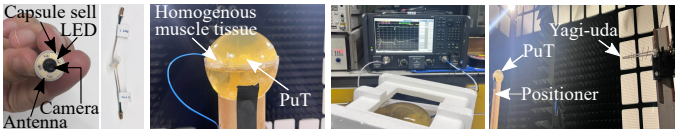

(a) (b) (c) (d) (e)

Fig. 12. (a) Camera-integrated planar antenna inside a capsule body. (b) Final capsule mockup containing components. (c) Capsule antenna mockup centered inside of a ø200 mm spherical phantom. (d) S-parameters characterization setup. (e) Far-field characterization setup inside of an anechoic chamber.

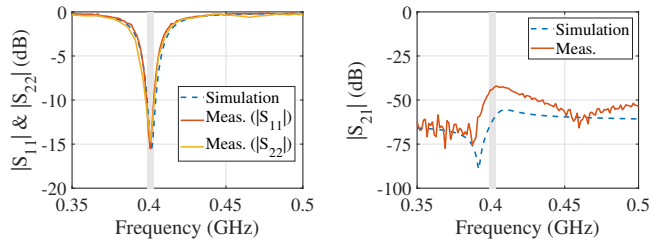

(a) (b)

Fig. 13. Measured and simulated S-parameters of the camera-integrated two-element MIMO capsule antenna in muscle tissue. (a) Magnitude of reflection coefficients $|S_{11}|$ and $|S_{22}|$. (b) Isolation $|S_{21}|$.

For optimal camera angles and high antenna performance, the presence of air within the airdrome at both ends of the capsule was considered during optimization [70]. A shell thickness of 0.5 mm was identified as optimal for efficient performance and minimal reflection, ensuring robustness and durability [71]. This approach allows detailed exploration of how different shell thicknesses affect antenna performance through the digestive system.

V. Realization and Measurements

A. Prototyping and Phantoms

Fig. 12(a) shows the MIMO antenna prototype. The printed antennas were soldered to 80-mm-long 50 Ω semirigid coaxial cables with SMA connectors. The antennas and other capsule components were placed in a 26 mm×11 mm capsule, as seen in Fig. 12(b). An opening on the cable side for measurement was sealed with Araldite 2011 epoxy paste.

For experimental characterization of the radiation and impedance, a muscle-equivalent solid phantom in a ø200 mm spherical container [Fig. 12(c)] was prepared using a water-sugar-salt-oil-gelatin formulation exploiting the formula in [72]. Gelatin was added to achieve a solid form, while a water-sugar-salt mix suffices for liquid phantoms [73]. The phantom's dielectric properties at 401 MHz were measured as $\epsilon_{tissue} = 57.5$ and $\sigma = 0.8$ S/m, using an Agilent measurement kit equipped with an 85070E coaxial probe [74].

B. Implantable Antenna Parameters

1) S-Parameters: The S-parameters were measured using a Keysight N5247B PNA-X microwave network analyzer. Fig. 12(d) shows the measurement setup, with the muscle-equivalent phantom fixed using Rohacell IG foam (ϵ_r = 1.05, tanδ = 0.0017). The SMA connectors were outside the container for easy measurement and de-embedding.

Fig. 13 presents the measured S-parameters and full-wave simulation results. The measured impedance bandwidth is 7 MHz, from 400 MHz to 407 MHz, covering the [401–406]MHz band. Throughout this band, isolation greater than 41 dB is maintained between the antennas, as shown in Fig. 13(b). Slight discrepancies between measured and simulated $|S_{21}|$ might be primarily due to challenges in soldering of cable for measurement, misalignment in laboratory environment, and maintaining consistent test conditions within the small capsule, which can affect signal integrity and antenna performance.

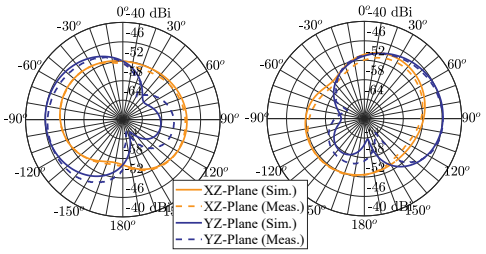

(a) (b)

Fig. 14. Measured and simulated radiation patterns of the proposed antennas positioned at the center of a homogeneous ø200 mm spherical phantom with muscle-equivalent EM properties at 401 MHz. (a) Antenna-1. (b) Antenna-2.

2) Radiation Performance: To characterize radiation performance, the pill-under-test (PuT) is placed at the center of a spherical muscle-equivalent phantom in an anechoic chamber. The PuT is illuminated in its far-field region by a Yagi-Uda antenna positioned 3 m away, as shown in Fig. 12(e). Radiation patterns for orthogonal planes are measured using a far-field antenna measurement system. At 401 MHz, the measured and simulated radiation patterns in the XZ- and YZ-planes agree well for both antennas, as shown in Fig. 14. A broadside gain of -46 dBi is achieved, with slight discrepancies due to measurement accuracy.

C. Link Margin

To assess the communication ability, distance coverage, and data-rate ability of the capsule antenna before implementing them in practical implants, it is essential to evaluate the link budget parameters between the capsule antenna and off-body/on-body receivers. The link margin (LM), the difference between available power R_a and required power R_r, can be computed as [75]

$$R_a[dB] = P_t + G_t + G_r - 10log_{10}(4\pi d/\lambda)^2, \quad (1)$$

$$R_r[dB] = E_b/N_o + 10log_{10}(B_r) + 10log_{10}(kT_o) - G_c + G_d, \quad (2)$$

where P_t is transmitter power, G_t is the gain of the capsule antenna, G_r = 2.18 dBi is the realized gain of an half-wave dipole antenna considered as a receiver antenna, d is the distance between capsule and receiver antenna, E_b/N_o = 9.6 dB is the ideal phase shift keying (PSK), k = 1.38×10^{-23} is the Boltzmann's constant, T_o = 273 K is the temperature, G_c = 0 dB is the coding gain, G_d = 2.5 dB is the fixing deterioration, and B_r is the bit rate which is taken as 1, 10, 25, 78, and 120 Mbps. The P_t is limited to 25 μW [32]. Yet, the system's performance is impacted as the data rate is directly related to P_t. Most WCE capsules use silver oxide coin batteries, providing 3 V at 55 mAh, lasting 8-10 hours, with a typical power transfer of 20 mW [76]. Although endoscopic antennas generally have low gains, input power must follow peak SAR restrictions [77]. Here, a P_t of 20 mW (13 dBm) is used based on SAR (10-g). The LM is calculated

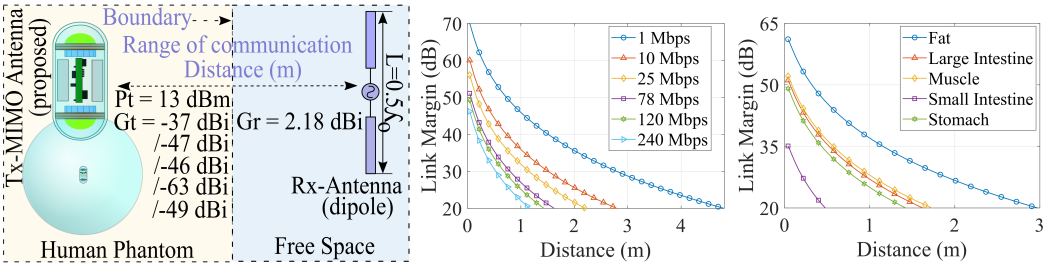

(a) (b) (c)

Fig. 15. Link margin analysis in different locations in GI tract for different transmission rates at 401 MHz. (a) A conceptual overview of the link analysis. (b) Link margins for different transmission rates. (c) Link margins in different locations for 78 Mbps data rate. For the fat, large intestine, muscles, small intestine, and stomach, the transmitter gain G_t values are -37 dBi, -47 dBi, -46 dBi, -63 dBi, -49 dBi, respectively.

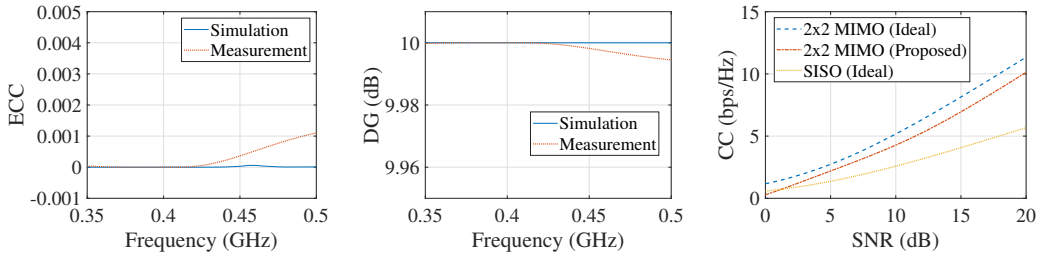

(a) (b) (c)

Fig. 16. MIMO channel parameters of the antenna: (a) Envelope correlation coefficients (ECC). (b) Diversity gain (DG). (c) Channel capacity (CC).

TABLE I
COMPARISON OF THE PROPOSED CAPSULE MIMO ANTENNA WITH THE STATE-OF-THE-ART CAPSULE MIMO ANTENNAS

Ref.	Antenna form	Frequency (MHz)	FBW (%)	Elements	Gain (dBi)	Isolation (dB)	ECC	AA (mm^2)	ID (mm)	Phantom: tissue, shape, size -, -, (mm^3)
[44]	C	2450	N.R.	2	N.R.	20*	N.R.	140	N.R.	Minced meat, rectangular, N.R.
[46]	C	915	14	4	-18.1	10	<0.4	471	65	Minced meat, cubic, 130×130×130
[41]	P	2450	13	2	-20.5	>28	<0.16	33.17	75	Minced meat, cubic, 150×150×150
[47]	P	2450	25.3	2	-20.6	30.1	0.11	21	80	Muscle, cubic, 160×160×160
[40]	P	433	33.9	2	-34.4	>26	0.1	100.3	90	Minced meat, rectangular, 130×130×46
T.W.	**P**	**401**	**1.8**	**2**	**-46**	**>41**	**<0.001**	**79.9**	**100**	**Muscle, spherical, ø200**

C.: Conformal; P: Planar; FBW: Fractional bandwidth; AA: Antenna area; ID: Implantation depth; *: Extracted from figure; N.R.: Not reported

by varying the distance between capsule and receiver antennas for different transmission rates and locations in the GI tract [see Fig. 15]. Ideally, an LM of 0 dB provides seamless communication, but in practice, an LM of 20 dB is considered effective. Fig. 15(b) shows that a high data rate of 120 Mbps is achievable within 1.2 m. Additionally, 78 Mbps can be transmitted over distances of 0.5 m, 1.4 m, 1.6 m, 1.7 m, and 3 m for an LM of 20 dB in the small intestine, stomach, large intestine, muscle, and fat, respectively [Fig. 15(c)]. Thus, the proposed antenna can provide a large LM at different GI tract locations for various transmission rates at 401 MHz. In real-time applications, the results show strong overall consistency with the calculations, with only slight deviations attributed to the transmission medium.

D. MIMO Channel Parameters

The main advantage of the MIMO antenna is its high channel capacity without needing extra bandwidth or power. The envelope correlation coefficient (ECC) evaluates MIMO channel independence, with ideal uncorrelated channels having ECC = 0, while values below 0.5 are acceptable in practice [78], [79]. Fig. 16(a) shows simulated and measured ECC values below 0.001, indicating suitability for high-data-rate WCE due to the distributed MIMO configuration. Diversity gain (DG) is another key MIMO parameter [80], [81] with uncorrelated channels typically achieving a DG of 10 dB. The proposed system achieves a DG above 9.99 dB across the operating band [Fig. 16(b)].

The channel capacity (CC) of the 2×2 MIMO antenna system, calculated using the formulations in [82], varies with the signal-to-noise ratio (SNR). As shown in Fig. 16(c), the proposed MIMO antenna's CC surpasses that of the SISO configuration. At SNR = 20 dB, it achieves a channel capacity of 10 bps/Hz, making it a promising choice for high-data-rate WCEs.

Table I compares the proposed MIMO antenna with state-of-the-art implantable designs, emphasizing its superior isolation. Despite lower gain from deep tissue penetration and compact size, it maintains a stable 7 MHz bandwidth across various tissue conditions in the [401–406] MHz MedRadio band, even with two integrated cameras and nearby components.

VI. CONCLUSION & FUTURE WORK

A novel dual-camera integrated two-element MIMO antenna using multilayer PCB technology is proposed, offering compact size, easy fabrication, and consistent bandwidth. Measurements show a -46 dBi gain covering the [401-406] MHz MedRadio band. Its small footprint and high isolation make it ideal for WCE capsules. Testing with an implantable capsule and components in a muscle-mimicking phantom showed an ECC below 0.001, DG over 9.99 dB, and a CC of 10 bps/Hz at 20 dB SNR across the band. In future work, we will explore a variety of modulation schemes for data transmission.

REFERENCES

[1] D. Panescu, "Emerging technologies [wireless communication systems for implantable medical devices]," *IEEE Eng. Med. Biol. Mag.*, vol. 27, no. 2, pp. 96-101, Mar./Apr. 2008.

[2] A. Kiourti and K. S. Nikita, "A review of implantable patch antennas for biomedical telemetry: Challenges and solutions [wireless corner]," *IEEE Antennas Propag. Mag.*, vol. 54, no. 3, pp. 210-228, Jun. 2012.

[3] A. F. Demir *et al.*, "In Vivo communications: Steps toward the next generation of implantable devices," *IEEE Veh. Technol. Mag.*, vol. 11, no. 2, pp. 32-42, Jun. 2016.

[4] M. Song *et al.*, "A millimeter-scale crystal-less MICS transceiver for insertable smart pills," *IEEE Trans. Biomed. Circuits and Syst.*, vol. 14, no. 6, pp. 1218-1229, Dec. 2020.

[5] G. Iddan, G. Meron, A. Glukhovsky, and P. Swain, "Wireless capsule endoscopy," *Nature*, vol. 405, pp. 417-418, May 2000.

[6] C. P. Swain, F. Gong, and T. N. Millis, "Wireless transmission of a color television moving image from the stomach using a miniature CCD camera, light source and microwave transmitter," *Gut*, vol. 39, no. A26, 1996.

[7] S. R. Khan, S. K. Pavuluri, G. Cummins, and M. P. Y. Desmulliez, "Wireless power transfer techniques for implantable medical devices: A review," *Sensors*, vol. 20, no. 12, p. 3487, Jun. 2020.

[8] Y. Zhou, C. Liu, and Y. Huang, "Wireless power transfer for implanted medical application: A review," *Energies*, vol. 13, no. 11, p. 2837, Jun. 2020.

[9] Y. Rahmat-Samii and L. Song, "Advances in communication and biomedical antenna developments at the UCLA antenna lab: Handheld, wearable, ingestible, and implantable [bioelectromagnetics]," *IEEE Antennas Propag. Mag.*, vol. 63, no. 5, pp. 102-115, Oct. 2021.

[10] G. Ciuti, A. Menciassi, and P. Dario, "Capsule endoscopy: From current achievements to open challenges," *IEEE Reviews in Biomed. Eng.*, vol. 4, pp. 59-72, 2011.

[11] A. Iqbal, A. Smida, A. J. Alazemi, M. I. Waly, N. K. Mallat, and S. Kim, "Wideband circularly polarized MIMO antenna for high data wearable biotelemetric devices," *IEEE Access*, vol. 8, pp. 17935-17944, 2020.

[12] L. Amjad, M. A. Hasan, I. B. Mabrouk, and M. Nedil, "Scalp implantable MIMO antenna for high-data-rate head implants," *IEEE Antennas and Wireless Propag. Lett.*, vol. 20, no. 12, pp. 2529-2533, Dec. 2021.

[13] M. K. Goenka, S. Majumder, and U. Goenka, "Capsule endoscopy: Present status and future expectation," *World J. Gastroenterol.,* vol. 20, no. 29, p. 10024, 2014.

[14] Jaeeun Jang *et al.*, "A four-camera VGA-resolution capsule endoscope system with 80-Mb/s body channel communication transceiver and sub-centimeter range capsule localization," *IEEE Journal of Solid-State Circuits,* vol. 54, no. 2, pp. 538-549, 2018.

[15] PillCam™ COLON 2 System. Accessed: Feb. 4, 2023. [Online]. Available: https://www.medtronic.com/covidien/en-us/products/capsule-endoscopy/pillcam-colon-2-system.html

[16] Y. Gu *et al.*, "Design of endoscopic capsule with multiple cameras," *IEEE Transactions on Biomedical Circuits and Systems,* vol. 9, no. 4, pp. 590-602, Aug. 2015.

[17] D. E. Yung *et al.*, "Double-headed small-bowel capsule endoscopy: Real-world experience from a multi-centre British study." *Digestive and Liver Disease,* vol. 53, no. 4, pp. 461-466, 2021.

[18] K. Triantafyllou *et al.*,"Two cameras detect more lesions in the small-bowel than one." *World journal of Gastroenterology,* vol. 17, no. 11, pp. 1462.

[19] K.N. Shim *et al.*, "Quality indicators for small bowel capsule endoscopy," *Clin Endosc,* vol. 50, no. 2, pp. 148-160, 2017.

[20] A.R. Robertson, D.E. Yung, S. Douglas, J.N. Plevris, A. Koulaouzidis, "Repeat capsule endoscopy in suspected gastrointestinal bleeding," *Scand J Gastroenterol,* vol. 54, no. 5, pp. 656-661, 2019.

[21] F. Kong, C. Qi, H. Lee, G. D. Durgin and M. Ghovanloo, "Antennas for intraoral tongue drive system at 2.4 GHz: Design characterization and comparison," *IEEE Trans. Microw. Theory Techn.*, vol. 66, no. 5, pp. 2546-2555, May 2018.

[22] C. Liu, Y.-X. Guo and S. Xiao, "Capacitively loaded circularly polarized implantable patch antenna for ISM band biomedical applications," *IEEE Trans. Antennas Propag.*, vol. 62, no. 5, pp. 2407-2417, May 2014.

[23] L.-J. Xu, Y. Bo, W.-J. Lu, L. Zhu and C.-F. Guo, "Circularly polarized annular ring antenna with wide axial-ratio bandwidth for biomedical applications," *IEEE Access*, vol. 7, pp. 59999-60009, 2019.

[24] D. Nikolayev, M. Zhadobov, and R. Sauleau, "Impact of tissue electromagnetic properties on radiation performance of in-body antennas," *IEEE Antennas Wireless Propag. Lett.*, vol. 17, no. 8, pp. 1440-1444, Aug. 2018.

[25] D. Nikolayev, M. Zhadobov, and R. Sauleau, "Immune-to-detuning wireless in-body platform for versatile biotelemetry applications," *IEEE Trans. Biomed. Circuits and Syst.*, vol. 13, no. 2, pp. 403-412, Apr. 2019.

[26] D. Nikolayev, W. Joseph, A. Skrivervik, M. Zhadobov, L. Martens, and R. Sauleau, "Dielectric-loaded conformal microstrip antennas for versatile in-body applications," *IEEE Antennas Wireless Propag. Lett.*, vol. 18, no. 12, pp. 2686-2690, Dec. 2019.

[27] G. Samanta and D. Mitra, "Dual-band circular polarized flexible implantable antenna using reactive impedance substrate," *IEEE Trans. Antennas Propag.*, vol. 67, no. 6, pp. 4218-4223, Jun. 2019.

[28] M. Zada, I. A. Shah and H. Yoo, "Metamaterial-loaded compact high-gain dual-band circularly polarized implantable antenna system for multiple biomedical applications," *IEEE Trans. Antennas Propag.*, vol. 68, no. 2, pp. 1140-1144, Feb. 2020.

[29] D. Nikolayev, A. K. Skrivervik, J. S. Ho, M. Zhadobov, and R. Sauleau, "Reconfigurable dual-band capsule-conformal antenna array for in-body bioelectronics," *IEEE Trans. Antennas Propag.*, vol. 70, no. 5, pp. 3749-3761, May 2022.

[30] K. Liu *et al.*, "Design of conformal spiral dual-band antenna for wireless capsule system," *IEEE Access*, vol. 9, pp. 117349-117357, 2021.

[31] F.-J. Huang, C.-M. Lee, C.-L. Chang, L.-K. Chen, T.-C. Yo and C.-H. Luo, "Rectenna application of miniaturized implantable antenna design for triple-band biotelemetry communication," *IEEE Trans. Antennas Propag.*, vol. 59, no. 7, pp. 2646-2653, Jul. 2011.

[32] M. Zada and H. Yoo, "A miniaturized triple-band implantable antenna system for bio-telemetry applications," *IEEE Trans. Antennas Propag.*, vol. 66, no. 12, pp. 7378-7382, Dec. 2018.

[33] A. Basir and H. Yoo, "Efficient wireless power transfer system with a miniaturized quad-band implantable antenna for deep-body multitasking implants," *IEEE Trans. Microw. Theory Techn.*, vol. 68, no. 5, pp. 1943-1953, May 2020.

[34] R. Das and H. Yoo, "A multiband antenna associating wireless monitoring and nonleaky wireless power transfer system for biomedical implants," *IEEE Trans. Microw. Theory Techn.*, vol. 65, no. 7, pp. 2485-2495, Jul. 2017.

[35] Z. Xia *et al.*, "A wideband circularly polarized implantable patch antenna for ISM band biomedical applications," *IEEE Trans. Antennas Propag.*, vol. 68, no. 3, pp. 2399-2404, Mar. 2020.

[36] A. Basir, M. Zada and H. Yoo, "Compact and flexible wideband antenna for intraoral tongue-drive system for people with disabilities," *IEEE Trans. Antennas Propag.*, vol. 68, no. 3, pp. 2405-2409, Mar. 2020.

[37] L. Cai, Z. Yang, M. Wang, H. Zheng, X. Wang and J. Liu, "Wideband antenna design and SAR comparison for electronic capsule endoscopy," *in Asia-Pacific Conf. on Antennas and Propag.*, Xi'an, China, Oct. 2017, pp. 1-3.

[38] J. Shang and Y. Yu, "An ultrawideband and conformal antenna for wireless capsule endoscopy," *Microw. Opt. Technol. Lett.*, vol. 62, pp. 860-865, 2020.

[39] A. Alemaryeen, "Compact wideband antenna for wireless capsule endoscopy system," *Appl. Phys. A.*, vol. 127, pp. 1-10, 2021.

[40] A. Iqbal, M. Al-Hasan, I. B. Mabrouk and M. Nedil, "A compact implantable MIMO antenna for high-data-rate biotelemetry applications," *IEEE Trans. Antennas Propag.*, vol. 70, no. 1, pp. 631-640, Jan. 2022.

[41] A. J. Alazemi and A. Iqbal, "A high data rate implantable MIMO antenna for deep implanted biomedical devices," *IEEE Trans. Antennas Propag.*, vol. 70, no. 2, pp. 998-1007, Feb. 2022.

[42] S. M. A. Shah, M. Zada, J. Nasir, O. Owais, A. Iqbal, and H. Yoo, "Miniaturized four-port MIMO implantable antenna for high-data-rate wireless-capsule-endoscopy applications," *IEEE Trans. Antennas Propag.*, vol. 71, no. 4, pp. 3123-3133, Apr. 2023.

[43] A. Iqbal and T. A. Denidni, "Two-element implantable MIMO antenna with sensing capabilities," *in IEEE Int. Symp. on Antennas and Prop. & USNC/URSI Nat. Radio Sci. Meeting,*, Denver, CO, USA, July 2022, pp. 99-100.

[44] L. Xu, B. Li, M. Zhang, and Y. Bo, "Conformal MIMO loop antenna for ingestible capsule applications," *Electron. Lett.*, vol. 53, no. 23, pp. 1506-1508, Nov. 2017.

[45] B. Biswas, A. Karmakar, and V. Chandra, "Hilbert curve inspired miniaturized MIMO antenna for wireless capsule endoscopy," *AEU Int. J. Electron. Commun.*, vol. 137, Jul. 2021, Art. no. 153819.

[46] Y. Wang, B. Huang and S. Yan, "A conformal four-antenna module for capsule endoscope MIMO operation," *IEEE Trans. Antennas Propag.*, vol. 70, no. 11, pp. 10270-10285, Nov. 2022.

[47] A. J. Alazemi1 and A. Iqbal, "A compact and wideband MIMO antenna for high-data-rate biomedical ingestible capsules," *Scientific Reports*, vol. 71, no. 4, pp. 3123-3133, Apr. 2023.

[48] J. J. Baek, S. W. Kim, and Y. T. Kim, "Camera-integrable wide-bandwidth antenna for capsule endoscope," *Sensors*, vol. 20, no. 1, pp. 1-7, 2020.

[49] J. J. Baek, S. W. Kim, and Y. T. Kim, "2.4 GHz wide-bandwidth inverted-F antenna for capsule endoscope," *Microw Opt. Technol Lett.*, vol. 62, pp. 1275-1280, 2020.

[50] K. Bazaka and M. V. Jacob, "Implantable devices: Issues and challenges," *Electronics*, vol. 2, no. 1, pp. 1-34, 2013.

[51] M. Bosiljevac, Z. Sipus, and A. K. Skrivervik, "Propagation in finite lossy media: An application to WBAN," *IEEE Antennas and Wireless Propag. Lett.*, vol. 14, pp. 1546-1549, 2015.

[52] D. Nikolayev, M. Zhadobov, L. Le Coq, P. Karban, and R. Sauleau, "Robust ultraminiature capsule antenna for ingestible and implantable applications," *IEEE Trans. Antennas Propag.*, vol. 65, no. 11, pp. 6107-6119, Nov. 2017.

[53] J.-H. Cho and S.H. Woo, Communication strategies for various types of swallowable telemetry capsules, [in Modern Telemetry], InTech Open, 2011, ch. 2, pp. 41-56.

[54] EMF-Portal-Avaliable: https:/www.emf-portal.org/en/cms/page/home/effects/radio-frequency

[55] Medical Device Radiocommunications Service (MedRadio). Accessed: May 7, 2023. [Online]. Available: https://www.fcc.gov/medical-device-radiocommunications-service-medradio

[56] M. Zada and H. Yoo, "Miniaturized dual band antennas for intra-oral tongue drive system in the ISM bands 433 MHz and 915 MHz: Design, safety, and link budget considerations," *IEEE Trans. Antennas Propag.*, vol. 67, no. 9, pp. 5843-5852, Sep. 2019.

[57] M. Zada, I. A. Shah, A. Basir, and H. Yoo, "Ultra-compact implantable antenna with enhanced performance for leadless cardiac pacemaker system," *IEEE Trans. Antennas Propag.*, vol. 69, no. 2, pp. 1152-1157, Feb. 2021.

[58] K. Gosalia, G. Lazzi, and M. Humayun, "Investigation of a microwave data telemetry link for a retinal prosthesis," *IEEE Trans. Microw. Theory Techn.*, vol. 52, no. 8, pp. 1925-1933, Aug. 2004.

[59] W. G. Scanlon, J. B. Burns, and N. E. Evans, "Compilation of the dielectric properties of body tissues at RF and microwave frequencies," *IEEE Trans. Biomed. Eng.*, vol. 47, no. 4, pp. 527-534, Apr. 2000.

[60] Z. Sipus, A. Šušnjara, A. K. Skrivervik, D. Poljak, and M. Bosiljevac, "Influence of uncertainty of body permittivity on achievable radiation efficiency of implantable antennas-stochastic analysis," *IEEE Trans. Antennas Propag.*, vol. 69, no. 10, pp. 6894-6905, Oct. 2021.

[61] M. Gao, Z. Sipus and A. K. Skrivervik, "Analytic approximation of in-body path loss for implanted antennas," *IEEE Open J. Antennas Propag.*, vol. 4, pp. 537-545, 2023.

[62] S. Gabriel, R. W. Lau, and C. Gabriel, "The dielectric properties of biological tissues: II. Measurements in the frequency range 10 Hz to 20 GHz," *Phys. Med. Biol.*, vol. 41, pp. 2251-2269, Nov. 1996.

[63] P. M. Izdebski, H. Rajagopalan, and Y. Rahmat-Samii, "Conformal ingestible capsule antenna: A novel chandelier meandered design," *IEEE Trans. Antennas Propag.*, vol. 57, no. 4, pp. 900-909, Apr. 2009.

[64] O. O. Olaode, W. D. Palmer, and W. T. Joines, "Effects of meandering on dipole antenna resonant frequency," *IEEE Antennas Wireless Propag. Lett.*, vol. 11, pp. 183-186, 2012.

[65] Product MiroCam® (Capsule Endoscope System). Link: https://bit.ly/2OwuHN2

[66] H. Q Ngo, A. Ashikhmin, H. Yang, E. G. Larsson, and T. L. Marzetta, "Cell-free massive MIMO versus small cells," *IEEE Trans. Wireless Comm.*, vol. 16, no. 3, pp. 1834-1850, Mar. 2017.

[67] CST Studio Suite 2019. Accessed: May 7, 2023. [Online]. Available: https://bit.ly/3fn96Um

[68] D. Nikolayev, M. Zhadobov, P. Karban, and R. Sauleau, "Electromagnetic radiation efficiency of body-implanted devices," *Phys. Rev. Appl.*, vol. 9, no. 2, Feb. 2018, Art. no. 024033.

[69] A. K. Skrivervik, "Implantable antennas: The challenge of efficiency," in *Proc. 7th Eur. Conf. Antennas Propag. (EuCAP)*, othenburg, Sweden, Apr. 2013, pp. 3627-3631.

[70] F. Merli, B. Fuchs, J. R. Mosig, and A. K. Skrivervik, "The effect of insulating layers on the performance of implanted antennas," *IEEE Trans. Antennas Propag.*, vol. 59, no. 1, pp. 21-31, Jan. 2011.

[71] A. K. Skrivervik, M. Bosiljevac, and Z. Sipus, "Fundamental limits for implanted antennas: Maximum power density reaching free space," *IEEE Trans. Antennas Propag.*, vol. 67, no. 8, pp. 4978-4988, Aug. 2019.

[72] T. Yilmaz, R. Foster, and Y. Hao, "Broadband tissue mimicking phantoms and a patch resonator for evaluating noninvasive monitoring of blood glucose levels," *IEEE Trans. Antennas Propag.*, vol. 62, no. 6, pp. 3064-3075, June 2014.

[73] E. Cil *et al.*, "On the use of impedance detuning for gastrointestinal segment tracking of ingestible capsules," *IEEE Trans. Antennas Propag.*, vol. 71, no. 2, pp. 1977-1981, Feb. 2023.

[74] Keysight dielectric probe kit. Accessed: December 12, 2023. [Online]. https://www.keysight.com/us/en/assets/7018-01196/technical-overviews/5989-0222.pdf

[75] W. Xia, K. Saito, M. Takahashi, and K. Ito, "Performances of an implanted cavity slot antenna embedded in the human arm," *IEEE Trans. Antennas Propag.*, vol. 57, no. 4, pp. 894-899, Apr. 2009.

[76] R. Das and H. Yoo, "A wideband circularly polarized conformal endoscopic antenna system for high-speed data transfer," *IEEE Trans. Antennas Propag.*, vol. 65, no. 6, pp. 2816-2826, Jun. 2017.

[77] A. Basir, M. Zada, Y. Cho, and H. Yoo, "A dual-circular-polarized endoscopic antenna with wideband characteristics and wireless biotelemetric link characterization," *IEEE Trans. Antennas Propag.*, vol. 68, no. 10, pp. 6953-6963, Oct. 2020.

[78] A. Iqbal, M. Al-Hasan, I. B. Mabrouk, and M. Nedil, "A compact implantable MIMO antenna for high-data-rate biotelemetry applications," *IEEE Trans. Antennas Propag.*, vol. 70, no. 1, pp. 631-640, Jan. 2022.

[79] M. Zada, I. A. Shah, and H. Yoo, "Integration of sub-6-GHz and mm-wave bands with a large frequency ratio for future 5G MIMO applications," *IEEE Access*, vol. 9, pp. 11241-11251, 2021.

[80] M. S. Sharawi, *Printed MIMO Antenna Engineering*. Norwood, MA, USA: Artech House, 2014.

[81] R. Tian, B. K. Lau, and Z. Ying, "Multiplexing efficiency of MIMO antennas," *IEEE Antennas Wireless Propag. Lett.*, vol. 10, pp. 183-186, 2011.

[82] D. Gesbert, M. Shafi, D. Shiu, P. J. Smith, and A. Naguib, "From theory to practice: An overview of MIMO space-time coded wireless systems," *IEEE J. Sel. Areas Commun.*, vol. 21, no. 3, pp. 281-302, Apr. 2003.